



Surface Structuring and Reverse Deposition of Nanoporous Titanium Oxides by Laser Ablation of Titanium in Air

V. P. Veiko¹ · Yu Yu Karlagina¹ · A. A. Samokhvalov¹ · D. S. Polyakov¹ · S. S. Manokhin² · M. M. Radaev¹ · G. V. Odintsova¹ · I. B. Gornushkin³

Received: 5 November 2021 / Accepted: 26 April 2022 / Published online: 18 May 2022
© The Author(s) 2022

Abstract

The deposition of titanium oxides during titanium laser ablation in air has been experimentally and numerically investigated. A titanium sample was irradiated by nanosecond pulses from an Yb-fiber laser with a beam scanned across the sample surface for its texturing. As a result, the hierarchical structure was observed consisting of a microrelief formed by the laser ablation and a nanoporous coating formed by the reverse deposition from the laser induced plasma plume. The chemical and phase composition of the nanoporous coating, as well as the morphology and structure of the surface, were studied using scanning electron microscopy, atomic force microscopy, and X-ray microanalysis. It was found that the deposit consists mostly of porous TiO₂ with 26% porosity and inclusions of TiO, Ti₂O₃, and Ti₂O₃N. Optical emission spectroscopy was used to control the plasma composition and estimate the effective temperature of plasma plume. The chemical-hydrodynamic model of laser induced plasma was developed to get a deeper insight into the deposition process. The model predicts that condensed titanium oxides, formed in peripheral plasma zones, gradually accumulate on the surface during the plasma plume evolution. A satisfactory agreement between the experimental and calculated chemical composition of the plasma plume as well as between the experimental and calculated composition and thickness of the deposited film was demonstrated. This allows a cautious conclusion that the formation of condensed oxides in the plasma and their consequent deposition onto the ablation surface are among the key mechanisms of formation of porous surface films.

Keywords Laser ablation · Laser induced plasma deposition · Surface coating · Titanium dioxide · Hydrodynamic model · Plasma chemistry · Emission spectroscopy

✉ I. B. Gornushkin
igor.gornushkin@bam.de

¹ ITMO University, Saint-Petersburg, Russia 197101

² Institute of Problems of Chemical Physics, Russian Academy of Sciences, Chernogolovka, Moscow oblast, Russia 142432

³ BAM Federal Institute for Materials Research and Testing, Richard-Willstätter-Strasse 11, 12489 Berlin, Germany

Introduction

Pulsed laser ablation is used to create micro- and nanoreliefs on metal surfaces. Different surface patterns like craters [1], grooves [2], periodical structures [3], random topology [4], and hierarchical reliefs can be obtained in this way. The hierarchical reliefs, i.e., microreliefs overlaid by nanoreliefs or by nanostructured coating were obtained on titanium surfaces by many researchers [5–8]. Both micro- and nanostructured hierarchical topology is of great importance in medical applications, e.g., for increasing a protein and a cell adhesion to the surface of dental implants [9–12] or for reducing bacterial colonization by adding antibacterial properties to the surface via special nanorelief [13, 14]. The authors of these works emphasize that such nanostructured coatings have strong potential for biological applications, particularly for titanium implants integrated into bone tissue. The microrelief with a subcellular size is essential for anchoring bone cells to a titanium surface, as demonstrated by Veiko et al. [15]. The cells “feel” the surface through integrins, the nanoscale cell membrane receptors [16]. To make a cell to sense a foreign titanium surface through the integrins, the surface must be coated with a biogenic substrate of attached proteins with nanoscale dimensions. Thus, the microrelief equipped with nano-roughness provides a closer contact and stronger bond of biogenic bone tissue to the non-biogenic titanium implant.

One of the important features of laser ablation of metals is a back deposition of evaporated atoms due to collisions in laser plasma. It was studied theoretically in several works [17, 18] for ablation in vacuum. The situation is different for ablation in air because evaporated metal atoms react with atmospheric gases (primarily oxygen) and reaction products set back onto a substrate surface. For ablation of Ti, this leads to a formation of a thin nanoporous layer of mainly titanium oxides that overlay the microrelief created by a laser [15]. The presence of such a layer improves the biocompatibility of Ti implants and makes such a version of local chemical vapor deposition (LCVD) process a promising technique for medical engineering.

The number of publications devoted to synthesis and applications of titanium dioxide shows nearly exponential growth since 2000 reaching twelve thousand in 2020 [19]. This demonstrates the high interest in this material. Regarding the methods based on laser ablation of Ti in oxygen-containing atmosphere, there are two groups of experimental works. In first, the influence of laser parameters and ambient conditions on physical and chemical properties of formed nanoporous layers and microreliefs is investigated. For example, Fathi-Hafshejani et al. [20] studied the effect of laser pulse duration between 5 and 2000 ns, pulse energy, and repetition rate on the formation of different phases of titanium dioxide. They have shown that longer pulse widths, slower scan speeds, and higher laser powers lead to the formation of the rutile phase, while shorter pulse widths, lower laser powers, and faster scan speeds result in the formation of anatase TiO₂. The works from the second group are focused on the dynamics of laser induced plasma plume and not on the deposition process. For example, Burakov et al. [21] investigated the spatial–temporal distribution of molecules in laser titanium plasma and showed that the formation of TiO molecules was due to the reactions between Ti atoms in the ground and metastable states and oxygen molecules. Parigger et al. [22] and Woods et al. [23] modeled a system of bands of TiO in laser plasma; they demonstrated experimentally that the lifetime of titanium monoxide molecule in laser plasma is about 100 μs. Itina et al. [24] developed a hybrid continuous-microscopic model of laser induced plasma plume expanding into a low-pressure gas atmosphere. The continuous, fluid dynamic part described the early, dense plasma plume stage and set the

initial conditions for the later, rarefied stage that was modeled by the atomistic direct simulation Monte Carlo (DSMC) method. The physical system was the titanium or aluminum substrates ablated into an oxygen atmosphere; a point of interest was mixing the ablated material with ambient gas. Chemical reactions were not included in the model.

To the best of our knowledge, there are no works, in which a relationship between the parameters of the laser plasma plume (i.e., density, temperature, and geometrical shape) and properties of the nanocoating redeposited back on the irradiated surface was investigated in detail. That is, the mechanisms of formation of nanostructures from laser induced plasma and their physicochemical properties are studied rather poorly, as well as a relationship between the chemical composition of the deposit and the conditions inside the plasma plume and the laser parameters. This problem can be solved quite effectively using computer simulations based on a physical–chemical model, which describes the formation and expansion of laser induced plasma plume, plasma chemistry, and processes on the target surface. However, such a complex model is not yet fully developed.

Many models of chemically active laser induced plasma have been proposed, but they are focused rather on specific aspects of the process than on the process in its wholeness. To name a few, Casavola et al. [25] developed a 2D fluid dynamic and chemical model to simulate laser induced ablation of titanium into atmospheric air. Titanium, titanium oxides, and other species were included into the chemical model to calculate the equilibrium composition of the plasma using a statistical thermodynamic approach based on partition functions. The mass flow from the ablation surface to plasma was introduced phenomenologically based on experimental data; however, no reverse mass flow was considered. Yan et al. [26] investigated the nanosecond laser ablation of titanium using a 2D axisymmetric plasma model combined with a thermal model of surface heating and material transport through a Knudsen layer. The change in the surface morphology was investigated as a function of laser fluence, although neither plasma chemistry nor redeposition of material on the ablation surface were considered. Morozov et al. [27] studied a back-flow of laser ablated material onto the ablation surface or a substrate using the test particle Monte Carlo method. Ablation of carbon into a low-pressure nitrogen atmosphere was modeled using a hard spheres approximation. A 100% sticking probability for adsorption of particle was assumed, no chemistry was considered. In contrast, chemistry was a central part of the model developed by Tsalikis et al. [28] who used a hybrid kinetic Monte Carlo (KMC) method for simulating silicon film growth in the process of plasma-enhanced chemical vapor deposition (PECVD). The KMC code was executed first to calculate a large set of chemical reactions and get an initial condition for the atomistic Monte Carlo code that optimized the structure of the film. However, PECVD usually assumes steady deposition conditions that are far from those in transient laser induced plasmas.

The goal of this work is, using a combination of experimental and theoretical methods, to study the key processes, which are responsible for deposition of titanium oxides from titanium laser induced plasma onto the ablation surface under atmospheric air conditions.

Experimental Technique

An Yb fiber laser is used for ablation of the Ti grade 2 samples. The schematic of the experimental setup is shown in Fig. 1 along with the illustration of the ablation process accompanied by chemical reactions and redeposition of material. The laser beam is focused by an f-theta objective and scanned across a sample surface using a galvanometric scanner. The laser

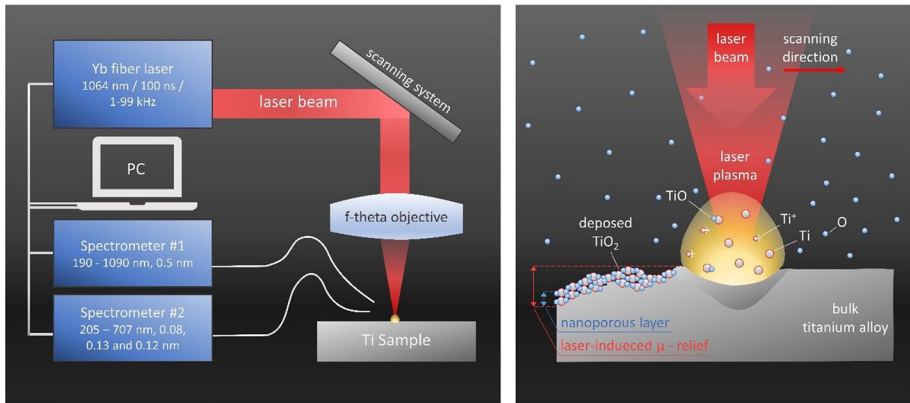


Fig. 1 Schematic representation of the experimental setup (left) and process of ablation and redeposition (right)

wavelength is 1064 nm, pulse duration is 100 ns, beam radius 25 μm , pulse energy 58–300 μJ , repetition rate 60 kHz, and beam scanning speed 50–100 mm/s. The laser fluence and irradiance are 3–15 J/cm^2 and $(0.3\text{--}1.5) \times 10^8 \text{ W}/\text{cm}^2$, correspondingly. The surface is scanned line-by-line with the distance between the lines of 30 μm . Such an operational mode provides the formation of a microrelief covered by a nanoporous layer of titanium oxides.

The temperature and composition of the plasma are determined from plasma emission spectra. Two miniature fiber-fed spectrometers are used: (i) Avantes ULS4096CL-EVO with a spectral range 190–1090 nm and resolution 0.5 nm to detect spectral bands of molecules with a high signal-to-noise ratio; and (ii) Avantes ULS-2048L 3-channel spectrometer with a spectral range 205–707 nm and spectral channel resolutions of 0.08, 0.13 and 0.12 nm to detect titanium ionic and atomic lines. The exposure time of the spectrometers is 10 ms and the spectra are averaged over 625 laser pulses to provide a high signal-to-noise ratio.

A scanning electron microscope (SEM) FEI Helios 660 in the electron and ion operational modes is used to study surfaces of structured specimens. A scanning transmission field-enhanced emission microscope (STEM) Tecnai G2 F20 is used to determine the phase composition of the deposit in a high-resolution TEM and electron diffraction analysis modes. The X-ray diffraction (XRD) analysis was performed using an ARL X'TRA diffractometer with the Bragg–Brentano focusing geometry and the following operational parameters: Cu-K α radiation at $\lambda = 1.5406 \text{ \AA}$, a 0.02° step size, $30^\circ\text{--}132^\circ$ 2θ range, and 1 s exposure time. Phase identification was performed using the databases [29, 30]. A detailed description of the sample preparation and phase compositional analysis can be found elsewhere [15]. Morphology of a single ablation crater is studied by an atomic force microscope (AFM) Nanoeducator.

Phenomenology of Ablation and Deposition and Plasma Model

Under the action of laser radiation, the titanium target melts and heats beyond the vaporization point that causes intense surface vaporization. A pool of molten material forms on the ablation surface. Due to the diffusive character of heat dissipation in material bulk, a size of the pool is limited to a size of the focused laser beam during first $10^{\text{'s}}$ ns $100^{\text{'s}}$ ns after the laser pulse. Plasma forms above the target surface and expands supersonically. This creates a

recoil pressure that leads to additional removal of material in the form of fine-dispersed liquid droplets. The recoil pressure also displaces the melt to edges of the ablation crater forming a ridge there. As the plasma cools down, chemical reactions start: first in the plasma periphery and later in plasma volume. Condensed products of the reactions return to the ablation surface being carried by a hydrodynamic flow. If ablation occurs in air, the titanium vapor interacts primarily with oxygen to produce titanium oxides of different stoichiometry in both gas and condensed phases. The production of oxides higher than TiO can also occur on a sample surface where the adsorbed TiO molecules can additionally oxidize.

Modeling the processes involved in this phenomenological description is a difficult task. In the model presented in this paper, as a first approximation, the laser-matter interaction is disregarded, and the model includes only the plasma plume expansion, chemical reactions, condensation, and accumulation of condensed species on the target surface. A zero time of the model corresponds to a time when the plasma plume has already been formed with a prescribed shape, temperature, and density. The thermodynamic and geometrical parameters for the initial plasma plume are taken from experiment.

A sequence of modeled events is the following. The plasma initially consists of titanium atoms, ions, and electrons. As it expands, titanium vapor reacts with molecules in the surrounding air. Some reactions lead to a formation of condensed species, a fraction of which settles on the target surface. Another fraction reflects from the surface and returns to the plasma plume. As time progresses, the condensed species accumulate within a surface area that is denoted as the deposition spot. The diameter of this spot is roughly ten times the size of the initial plasma.

A framework for the hydrodynamic part of the model is described by Shabanov and Gornushkin [31, 32] and the chemical part by Gordon and McBride [33]. In brief, plasma is in local thermodynamic equilibrium, LTE. The hydrodynamic flow is modeled via a system of Navier–Stokes equations, which include a surface source and sink to account for material removed by vaporization and accumulated on the surface as a deposit. The chemical part is based on the equilibrium model, which is embedded into the hydrodynamic code.

It should be emphasized that during first 10's ns after the breakdown the laser induced plasma may not be at LTE [34]. But later, when the characteristic time of the hydrodynamic flow becomes longer than the characteristic time for chemical reactions, the plasma approaches the equilibrium state. Establishing chemical equilibrium is fast in the atmospheric plasmas; the dense collisional environment makes LTE a reasonable assumption there [35].

Chemical equilibrium is solved by the minimization of the Gibbs free energy. The plasma is assumed axisymmetric; the cylindrical coordinates are used to solve the hydrodynamic equations. The material transport between the plasma and the ablation surface and other theoretical details are provided in the accompanying paper [36]. As far as the authors know, it is a first attempt to use a combined hydrodynamic-chemical model to study a chemical composition of condensed titanium oxides redeposited on the ablation titanium surface from a nanosecond laser ablation plasma in atmospheric air.

Results and Discussion

Properties of Plasma Plume and Surface Coating

Plasma emission spectra obtained at different laser fluences are shown in Fig. 2. In a short-wavelength range of 330–440 nm (Fig. 2a), only emission lines of titanium atoms and ions

are observed. In a long-wavelength range of 560–880 nm (Fig. 2b), strong bands B–X, A–X, and E–X systems of titanium monoxide TiO are identified [35]. A threshold for the appearance of molecular bands is about 3 J/cm^2 (see the inset in Fig. 2b), the same as for the appearance of titanium lines. The bands of TiO appear at a late stage of plasma evolution; the emission lifetime of this molecule is about $10 \mu\text{s}$ [37]. For the highest tested fluence of 15 J/cm^2 , bremsstrahlung continuum dominates the spectrum at early times [38]. The continuum emission adds to the line discrete spectrum that forms later. The main emitting species are the titanium atoms and ions and titanium monoxide molecules.

The average temperatures of laser induced plasmas corresponding to different laser fluences are calculated by the Boltzmann plot method [39]. A relation $\ln(\lambda I/g_k A_{ki}) = -E_k/kT$ is used, where I is the line integral intensity, λ is the wavelength at a line center, A_{ki} is the Einstein coefficient for spontaneous emission, and g_k and E_k are the degeneracy and energy of the upper transition state. The parameters A_{ki} , g_k , and E_k are taken from [40]. Figure 3a shows the spectral fragments with titanium lines marked, which were used for the construction of the Boltzmann plots. Figure 3b shows the Boltzmann plots constructed for plasmas obtained at laser fluences between 4.5 and 15 J/cm^2 that corresponds to the average plasma temperatures between 6700 and 7000 K .

Figure 4 shows the SEM images of the titanium surface obtained by ablation of the pure titanium target at different laser fluences and effective exposure times. The effective exposure time is a product of the number of laser pulses delivered to the surface and the pulse duration. An increase in the laser fluence from 5 to 15 J/cm^2 at a fixed effective exposure time of $0.1 \mu\text{s}$ leads to agglomeration of nanosized oxide particles on the exposed surface (Fig. 4a). An increase in the exposure time from 0.5 to $15 \mu\text{s}$ at a fixed fluence of 5 J/cm^2 leads to the formation of a quasi-homogeneous volumetric nanorelief (Fig. 4b) with a denser particle arrangement in comparison with the fixed exposure time/ fluence increase situation.

A similar study was performed by Fathi-Hafshejani [20] in controlled oxygen atmosphere; they showed that not only the relief but also the phase of TiO_2 depends on parameters of the laser scan: the longer pulse width, slower scan speed, and higher laser power led to the formation of rutile phase, while shorter pulse width, lower laser power, and faster scan speed resulted in the formation of anatase TiO_2 . Surface morphology was studied

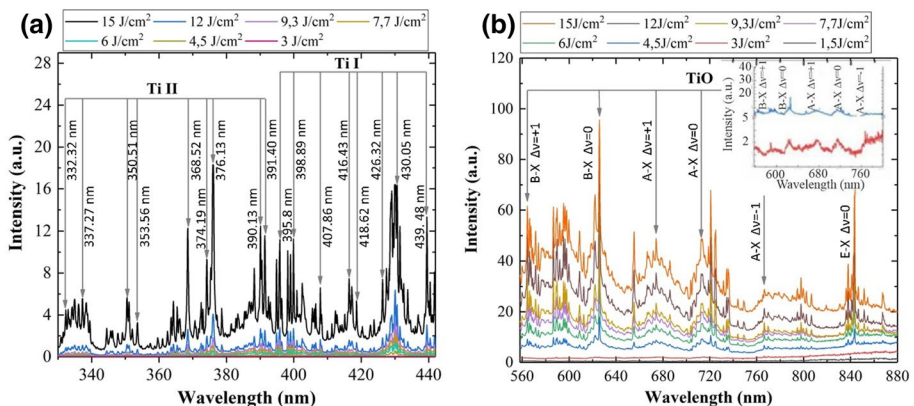


Fig. 2 **a** Emission spectra of laser plasma in spectral range 330–440 nm; **b** emission spectra of laser plasma in spectral range 560–880 nm

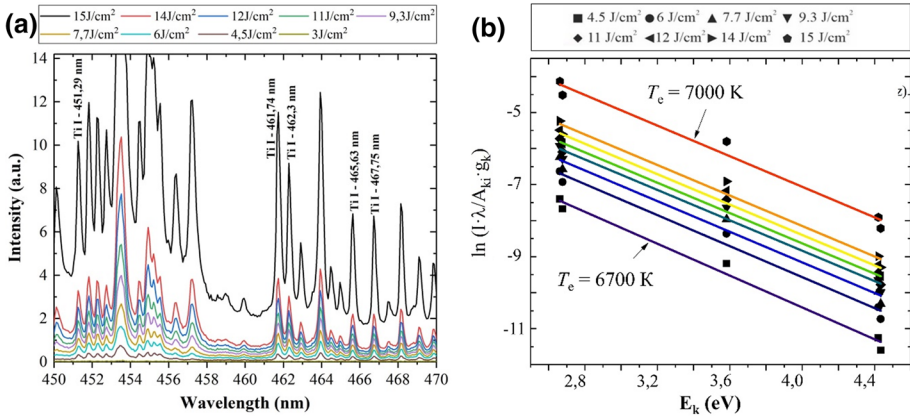


Fig. 3 **a** Fragment of titanium plasma spectrum with labeled lines used for construction of Boltzmann plots; **b** Boltzmann plots corresponding to different laser fluences

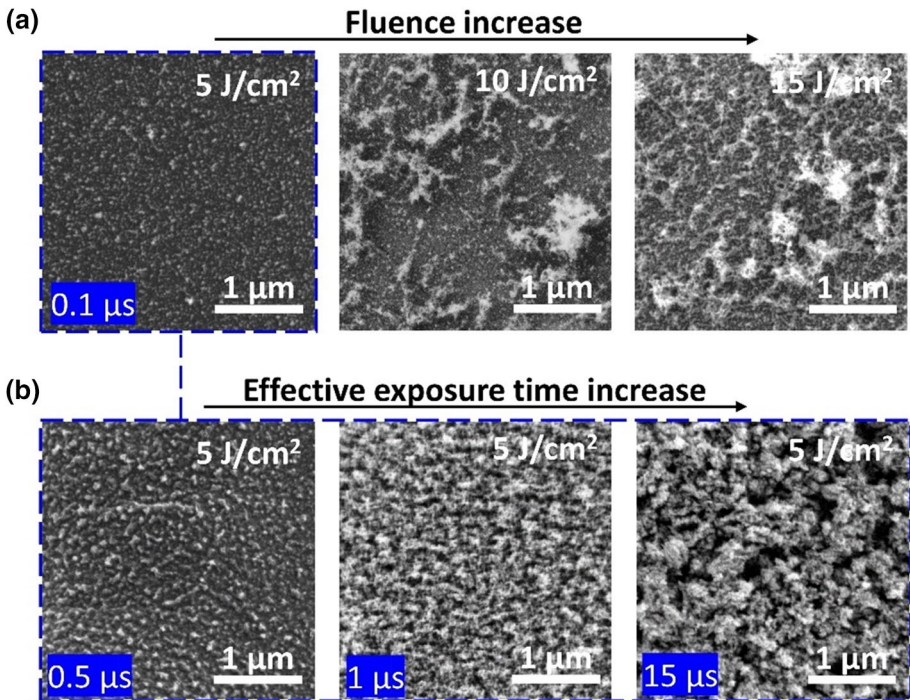


Fig. 4 **a** SEM images of titanium surface after laser ablation at fluences 5, 10, and 15 J/cm²; **b** SEM images of titanium surface after laser ablation at fluence 5 J/cm² (irradiance 5.1×10^7 W/cm²) and effective exposure times of 0.5, 1, and 15 μs

by Lee et al. [6] for a nanosecond ablation of titanium with a UV laser; the morphology varied significantly with a laser travel speed, from the groove-like structure with a width of ~5–10 μm and depth-to-width ratio of 4.6 for a low, 10 mm/s, scan speed to the shallow

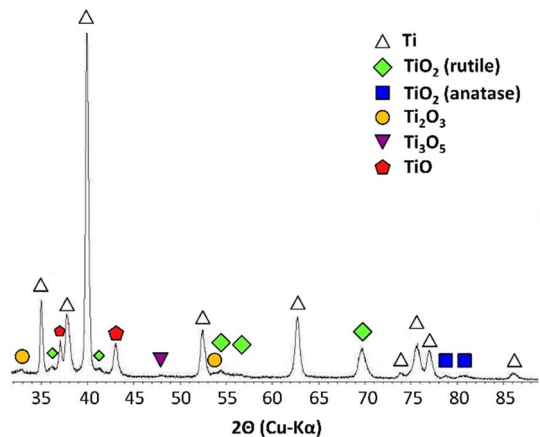
wave-like structure with a width of $\sim 11\text{--}20\ \mu\text{m}$ and a depth-to-width ratio of 0.3 for a high, 300 mm/s, travel speed.

The X-ray diffraction analysis was performed for the near-surface layer (several micrometers) of the sample, which was processed by scanning the laser pulses at a fluence of $5\ \text{J}/\text{cm}^2$ and effective exposure time of $1\ \mu\text{s}$. As can be seen from the obtained XRD spectrum (Fig. 5), there are several intense peaks that belong to $\alpha\text{-Ti}$ and $\beta\text{-Ti}$ [41]. They come from the titanium substrate underlying the deposit material. The attribution of these and other peaks is verified using many previously reported data [12, 42–45].

The composition of the deposit strongly depends on experimental conditions. For example, Landis et al. [46] textured titanium with a 805 nm Ti:sapphire femtosecond laser at a $0.25\ \text{J}/\text{cm}^2$ fluence ($2.5 \times 10^{12}\ \text{W}/\text{cm}^2$ irradiance) in oxygen and found, based on Raman spectroscopy, that the deposit consisted of predominantly amorphous TiO_2 with small inclusion of Ti_2O_3 . Křenek et al. [12] ablated titanium with a 200 ns laser (1064 nm) at a fluence of $24\ \text{J}/\text{cm}^2$ (irradiance of $1.2 \times 10^8\ \text{W}/\text{cm}^2$) and reported crystalline fractions of hongquite ($>35\%$), $\alpha\text{-Ti}$ (15–20%), Ti_2O_3 (10–15%), Ti_3O (15–20%) and minor anatase and rutile (together 5%). It is, however, unclear how to interpret this percentage composition obtained from the spectrum, which contains peaks of both the deposit and the substrate. Regarding the qualitative composition of the deposit, our results coincide with that in [12, 42]. Considering the peak intensities on the X-ray diffraction spectrum, we suggest that the main components of the deposited material are TiO_2 and TiO with impurities of Ti_3O_5 and Ti_2O_3 .

For a more detailed study of the structure and composition of the titanium alloy surface after laser ablation, a spherical microparticle covered by nanoporous material was chosen. Figure 6a presents the magnified SEM image of the laser-produced hierarchical relief which is obtained using a fluence of $5\ \text{J}/\text{cm}^2$ and irradiance $5.1 \times 10^7\ \text{W}/\text{cm}^2$. Using the focused ion beam (FIB) thinning, a thin foil containing a spherical microparticle (see the inset in Fig. 6a) with a sprayed protective platinum layer was cut in the SEM column (Fig. 6b) and examined by TEM (Fig. 6c). The STEM image in Fig. 6c shows that the upper layer of the microparticle has the porous structure with a pore size of about 500 nm. This layer, which extends from the green to blue dashed lines in Fig. 6c, according to high-resolution TEM analysis and electron diffraction analyses (Fig. 6d), consists of agglomerated rutile nanoparticles of about 5 nm in diameter (Fig. 6a). The lower porous layer, which

Fig. 5 XRD analysis of the titanium surface after laser ablation at fluence of $5\ \text{J}/\text{cm}^2$ (irradiance $5.1 \times 10^7\ \text{W}/\text{cm}^2$) and effective exposure time of $1\ \mu\text{s}$. The spectrum contains Ti, TiO_2 (rutile and anatase), TiO , Ti_2O_3 , and Ti_3O_5 peaks



extends from the blue to red dashed lines in Fig. 6c, has the columnar texture and consists of both rutile and anatase. The analysis reveals that the nanoporous coating is made of two layers differing in the content of TiO_2 and phase and morphology of the pores. The main component of the deposit is TiO_2 . The deposit, in turn, lies on a layer of a non-porous grained material that consists of TiO (Fig. 6e). The main volume of the microparticle is occupied by the non-porous grained TiO . The close inspection of the STEM image reveals a transitional layer between the TiO interior and TiO_2 exterior of the microparticle that differs from them by contrast; it extends from the red to yellow dashed lines in Fig. 6f. This non-porous layer consists of Ti_2O_3 and contains a thin layer of $\text{Ti}_2\text{O}_3\text{N}$ as described in Veiko et al. [15].

This result is consistent with that of Křenek et al. [12] who analyzed the sub- μm accretions developed on the surface of μm -sized round shape particles by the HRTEM and electron diffraction and found that the accretions contained crystalline rutile, anatase, brookite, Ti_3O_5 , TiO and Al_2O_3 nanoparticles. The round shape of the particles was explained by the rapid solidification of ejected hot liquid drops, however, it remained unexplained how such the complex composition of the particles could be formed.

The porosity of the oxide coating is evaluated from the STEM image. After processing the image with software (Fig. 7a), a ratio of white to black pixels is calculated. The porosity is estimated at about 26%. The same image is used for evaluation of an average height of the oxide coating; it is found to be $1.60 \pm 0.35 \mu\text{m}$ ($\alpha = 0.95$, $t_{\text{cn}} = 1.697$).

The mass of titanium ablated in a single pulse is evaluated by measuring a crater volume by AFM. The scan of the crater created by the 15 J/cm^2 laser pulse is shown in Fig. 8. The crater volume is equal to a difference between the full crater volume and a volume of

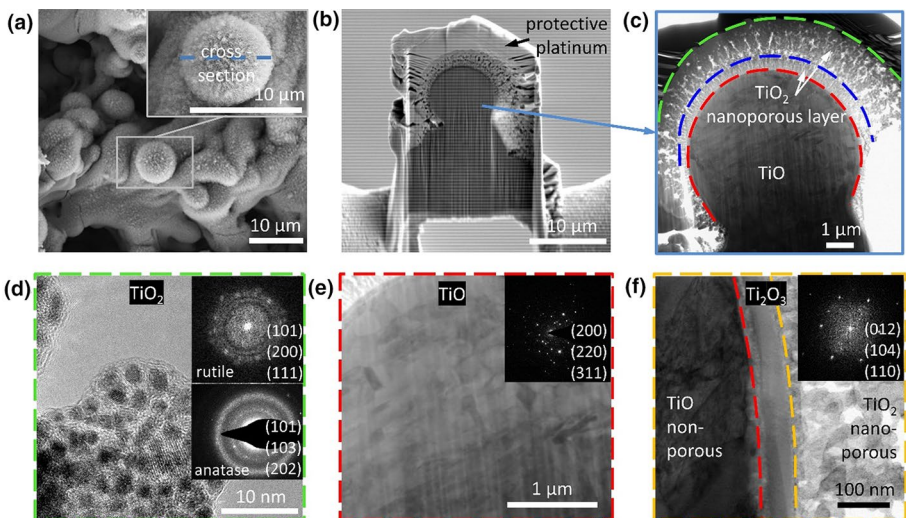


Fig. 6 SEM images of titanium sample after laser processing: **a** top view of the structured surface; the inset shows a magnified view of the spherical microparticle covered by the nanoporous coating; **b** cross-section of the spherical microparticle after FIB thinning; **c** STEM image of the microparticle; **d** high-resolution image of the nanoporous coating; **e** magnified view of the central cross section of the microparticle **f** magnified view of the transitional layer between the nanoporous exterior coating and non-porous interior material of the spherical microparticle; the insets show a Fourier transform scheme. Rutile nanoparticles have a size of about 5 nm (Color figure online)

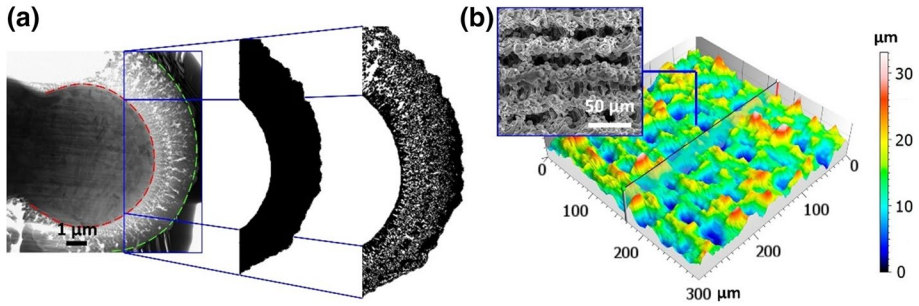


Fig. 7 **a** Evaluation of porosity and average height of oxide coating from the STEM image; **b** 3D profilometry of the laser-produced relief

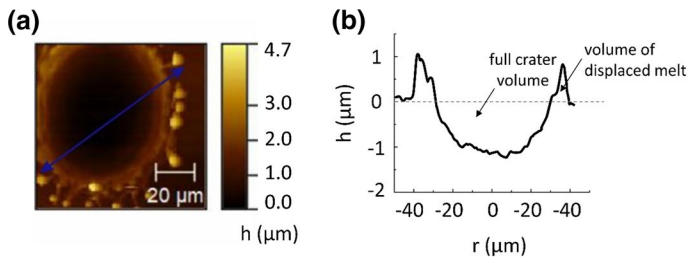


Fig. 8 **a** 2D AFM scan of ablation crater; **b** corresponding crater profile

the ridge at a crater edge (Fig. 8b). The mass evaporated by a single pulse is estimated at about 5 ng.

Simulation of Chemical Composition of Plasma Plume and Deposited Layer

The initial plasma plume consists of pure titanium surrounded by atmospheric air at 1 bar pressure. The air is approximated by three components, $N_2/O_2/Ar = 78/21/1$. A list of considered chemical species is given in Table 1. The TiN molecule was excluded from the simulation as it was not found in the deposit.

In the HD simulation, titanium vapor enters the plasma from a hot surface at a rate of 1 ng/μs. The vapor comes from a surface spot having an area equal to the area of the focused laser beam, $2 \times 10^{-5} \text{ cm}^2$. The spot temperature is set to the boiling temperature of titanium, 3560 K, while the rest of the surface is kept at the room temperature of 300 K. The initial plasma shape is semi-ellipsoidal with semi-axes 25 μm and 50 μm along the lateral and vertical directions, correspondingly. The 5-ng ablated mass is uniformly distributed over the volume with a density of 0.076 g/cm^3 . The initial plasma temperature is set to 7000 K as suggested by experiment.

Condensed particles, which form within a boundary layer at the interface between the plasma and the surface are assumed to have a sticking probability of 0.2, a reasonable number suggested by the literature [28, 47]. Those particles, which do not adsorb at the surface, reflect from it, and are carried away by the hydrodynamic flow. The value of 0.2 for the sticking coefficient can be a parameter of the model, which is found from the fitting of the

Table 1 Species participating in equilibrium calculations

Gaseous species	
Atoms and ions	Ti, T ⁺ , Ti ⁻ , Ar, Ar ⁺ , N, N ⁺ , N ⁻ , O, O ⁺ , O ⁻ , N ₂ , N ₂ ⁺ , N ₂ ⁻ , N ₃ , O ₂ , O ₂ ⁺ , O ₂ ⁻ , O ₃
Nitrogen oxides	NO, NO ⁺ , NO ₂ , NO ₂ ⁻ , NO ₃ , NO ₃ ⁻ , N ₂ O, N ₂ O ⁺ , N ₂ O ₃ , N ₂ O ₄ , N ₂ O ₅
Titanium oxides	TiO, TO ⁺ , TiO ₂
Condensed species	
Titanium and titanium oxides	Ti(a), Ti(b), Ti(L), TiO(a), TiO(b), TiO(c), TiO(L), TiO ₂ (cr), TiO ₂ (L), Ti ₂ O ₃ (l), Ti ₂ O ₃ (L), Ti ₃ O ₅ (a), Ti ₃ O ₅ (b), Ti ₃ O ₅ (L), Ti ₄ O ₇ (cr), Ti ₄ O ₇ (L)
Titanium nitrides	TiN(cr), TiN(L)

calculated and measured thickness of the deposit. The condensed species accumulate on the surface during the entire plasma lifetime that is the computational time.

Figure 9 a and b show the composition of the plasma gaseous species. The hot plasma core consists of mostly atomic and ionic species and strongly bound molecules of titanium oxide and nitrogen. Closer to periphery, in a zone of strong mixing with air, the number of molecular species increases while the number of elemental species decreases. The higher titanium oxides, TiO₂, Ti₃O₅, and Ti₄O₇, form here in both liquid and crystalline phases.

Figure 9, c and d show the mass deposited on the sample surface by the 20th and 230th ns of plasma evolution. Each point on the plots corresponds to a total mass accumulated on a surface layer between r and $r + \Delta r$ where Δr is the spatial discretization step. Calculations are interrupted at the 230th ns because beyond this point the deposition of material nearly stops. Figure 9d shows that the most active zone of production of condensed titanium oxides lies between 0.05 and 0.20 mm whereas a zone of formation of liquid titanium is above the molten pool between 0 and 0.025 mm (note the logarithmic scale on the y-axis). Such the distribution of the deposit produces a non-uniform coating around the ablation crater. In a scanning ablation mode, when many deposition spots overlay, the thickness of the deposit increases, and porosity develops due to non-uniformity of the single-pulse deposition.

Comparison of Simulation and Experiment

The yield of the deposition of TiO₂ per a pulse can roughly be estimated from the data in Fig. 9d. It is also possible to estimate a height of the deposit that is obtained in a scanning ablation regime using the instrumental settings given in the experimental section. A method to estimate the height of the deposit is illustrated in Fig. 10.

The deposition spot is defined as a circle around the ablation crater, inside which the mass of the deposit exceeds 0.1 μg . From Fig. 9d, the radius of the circle is 200 μm . The amount of material deposited during the scan is determined by the intersection of multiple deposition spots as shown in Fig. 10a. The distribution of the thickness of the single-pulse deposit within the deposition circle is shown in Fig. 9b. It is a 2D version of the mass distribution shown in Fig. 9d. The thickness of each concentric layer is calculated via $h_i = \mu_i / \rho$ where h_i is the height of the deposition layer between radii r_i and r_{i+1} , $\mu_i = m_i / \pi r_i \Delta r$ is the mass surface density inside this layer, and ρ is the density of the titanium dioxide (the deposit).

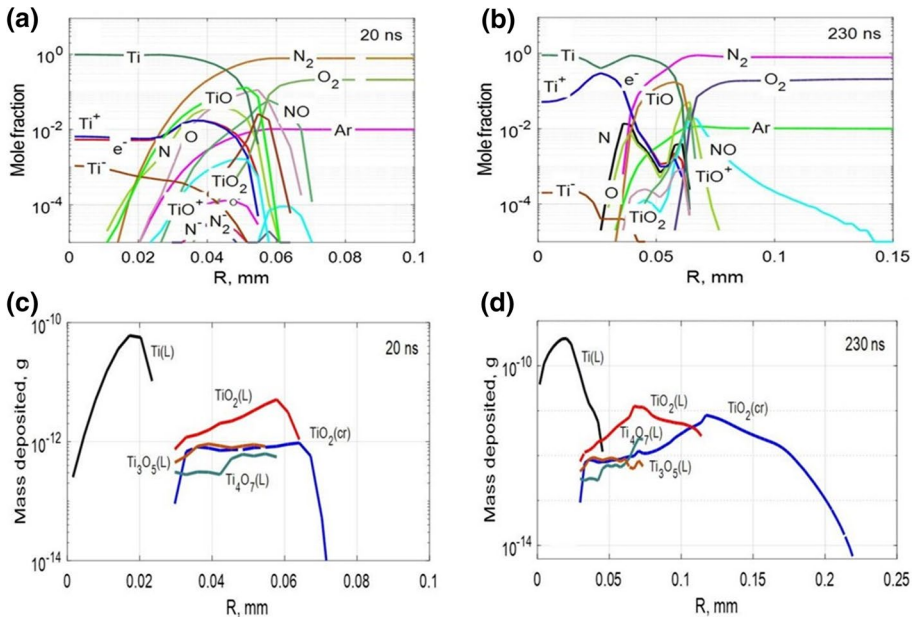


Fig. 9 Equilibrium composition of gaseous plasma species at 20 ns (a) and 230 ns (b) of plasma evolution; c condensed species accumulated on the surface by 20th ns (c) and 230th ns (d) of plasma evolution

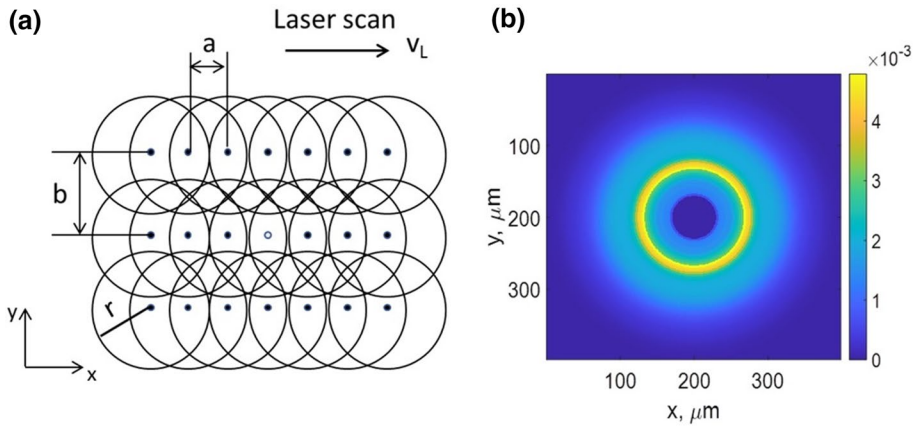


Fig. 10 a Illustration of the deposition in the scanning laser mode: *a* and *b* are the distances between craters in *x* and *y* directions; *v_L* is the laser scan speed, and *r* is the radius of the deposition spot; b thickness of the single-pulse deposit; the scale in the color bar is in μm

The calculated thickness of the deposit created on a 1000 × 1000 μm² scanning area is shown in Fig. 10 for two scan speeds: 10 cm/s (experimental) and 180 cm/s (hypothetical).

The distance between the craters in the *y*-direction is 30 μm for both the cases whereas in the *x*-direction it is only 1.7 μm for *v_L* = 10 cm/s (Fig. 11a) and 30 μm for *v_L* = 180 cm/s (Fig. 11b). The large overlap of the deposition spots with diameters of 400 μm leads to a creation of the 2.3 μm-thick layer of TiO₂ at the scanning speed of 10 cm/s. The fine

structure of this layer is shown in the inset in Fig. 11a. Separate craters cannot be discerned; only shallow trenches are seen in the y-scan direction. This picture is consistent with the SEM image shown in Fig. 7b; the similarity of the patterns is apparent. The predicted thickness of $2.3 \mu\text{m}$ is also close to the average deposit thickness of $1.60 \pm 0.35 \mu\text{m}$ measured in experiment. At a higher (hypothetical) speed of 180 cm/s (Fig. 11b) the deposition layer is more than 10 times thinner, only $0.14 \mu\text{m}$ in height, but single craters are clearly discerned. This example demonstrates that various surface patterns can be created by varying the scan speed. From the insets in Fig. 11 a, b one infers that the porosity of the deposited layers is a consequence of a non-uniform mass distribution across the overlapping deposition spots.

To resume, the developed model reproduces the main features of the obtained experimental data, namely, (i) the composition of the plasma plume in the model (Fig. 9a, b) coincides, for measurable species, with that found by spectroscopy in the real plasma (Fig. 2). In both cases, the major plasma components are titanium atoms and ions, titanium monoxide, and atmospheric species. (ii) The model correctly predicts one major component of the deposit, the crystalline TiO_2 . The discrepancy occurs for TiO and minor components: instead of Ti_3O_5 and Ti_4O_7 in the model, the minute amounts of TiO , Ti_2O_3 , and $\text{Ti}_2\text{O}_3\text{N}$ are detected in experiment. This can be explained by the absence of $\text{Ti}_2\text{O}_3\text{N}$ in the database (Table 1), disregarding chemical kinetics, and, possibly, imprecise initial conditions. (iii) The model yields the value for the thickness of the deposit that is close to the experimental value.

Conclusions

The paper demonstrates that the intense nanosecond laser ablation of titanium in air leads to the formation of a thin nanoporous layer deposited on a substrate surface from an expanding ablation plume. The layer consists mainly of titanium dioxide with 26% porosity. A hierarchical microrelief covered by the $2 \mu\text{m}$ -thick, porous deposit oxide layer is

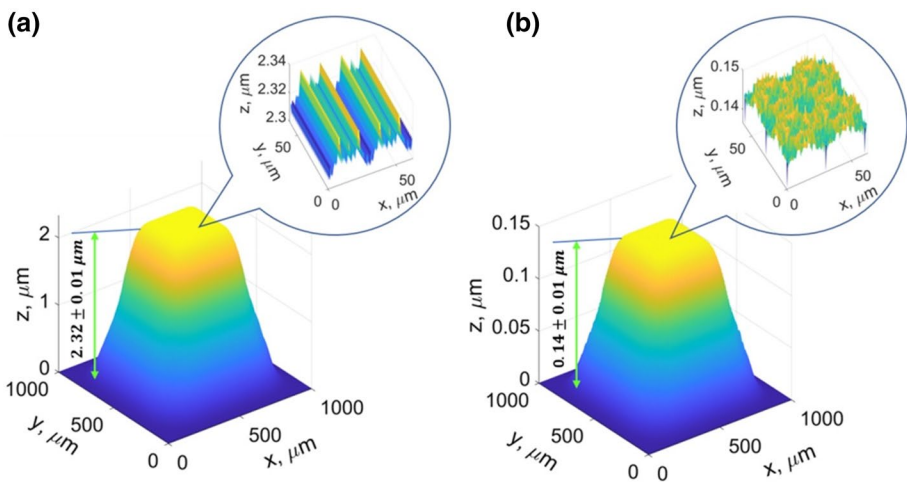


Fig. 11 **a** Layer of TiO_2 deposited onto an area $1000 \times 1000 \mu\text{m}^2$ at the scan speed 10 cm/s ; **b** the same at the scan speed 180 cm/s . The insets show the fine structures on tops of the deposits

produced by scanning the laser along parallel lines separated by 30 μm . For better understanding of the deposition process, the computer simulation of the process is performed using a fluid dynamic plasma model coupled with the equilibrium chemical code.

Based on the experimental observations and model simulations, the following qualitative picture of the deposition of titanium oxides under nanosecond laser ablation of titanium in air can be proposed. The plasma plume created by the laser pulse with the initial temperature of ~ 7000 K and density ~ 0.08 g/cm³ rapidly expands and cools down. Chemical reactions in the hot plasma zone result in formation of strongly bound molecules of titanium monoxide, whose spectral lines are observed in the experiment. In a due course of the plasma expansion and cooling, TiO₂ molecules form in a colder peripheral plasma zone where Ti and TiO species actively mix with surrounding air. The phase composition of TiO₂, which is localized near the surface during the plume expansion, consists of gaseous, liquid, and crystalline species. A fraction of these species adheres to the cold surface at a certain lateral distance from the center of the irradiated spot and form a nanoporous layer observed in the experiment. Overall, it can be concluded that the deposition of condensed metal oxides from plasma to the ablation surface is among the most important mechanisms of formation of nanoporous oxide films on metal surfaces. The results reported here allow for the deeper understanding of this mechanism. The experimental method studied has a potential to be developed into a useful technology that can find applications in medicine, photonics, and other fields.

Acknowledgements The study was supported by the Russian Science Foundation (Project 20-62-46045). I.G. thanks Prof. U. Panne and Dr. K. Rurack for supporting this work.

Funding Open Access funding enabled and organized by Projekt DEAL.

Open Access This article is licensed under a Creative Commons Attribution 4.0 International License, which permits use, sharing, adaptation, distribution and reproduction in any medium or format, as long as you give appropriate credit to the original author(s) and the source, provide a link to the Creative Commons licence, and indicate if changes were made. The images or other third party material in this article are included in the article's Creative Commons licence, unless indicated otherwise in a credit line to the material. If material is not included in the article's Creative Commons licence and your intended use is not permitted by statutory regulation or exceeds the permitted use, you will need to obtain permission directly from the copyright holder. To view a copy of this licence, visit <http://creativecommons.org/licenses/by/4.0/>.

References

1. Ahmed N, Darwish S, Alahmari AM, Salik K (2015) *Mater Manuf Process* 30:1290–1297
2. Zhao W, Wang L, Yu Z, Chen J, Yang J (2019) *Opt Laser Technol* 111:214–221
3. Gemini L, Hashida M, Miyasaka Y, Inoue S, Limpouch J, Mocek T, Sakabe S (2015) *Appl Surf Sci* 336:349–353
4. Demir AG, Maressa P, Previtali B (2013) *Phys Procedia* 41:759–768
5. Zwahr C, Helbig R, Werner C, Lasagni AF (2019) *Sci Rep* 9:6721
6. Lee H-T, Lin C-C (2019) *Mater Trans* 60:1799–1806
7. Shah FA, Johansson ML, Omar O, Simonsson H, Palmquist A, Thomsen P (2016) *PLoS ONE* 11:e0157504
8. Palmquist A, Lindberg F, Emanuelsson L, Brånemark R, Engqvist H, Thomsen P (2010) *J Biomed Mater Res A* 92:1476–1486
9. Kopf BS, Ruch S, Berner S, Spencer ND, Maniura-Weber K (2015) *J Biomed Mater Res A* 103:2661–2672
10. Raimbault O, Benayoun S, Anselme K, Maclair C, Bourgade T, Kietzig A-M et al (2016) *Mater Sci Eng C* 69:311–320

11. Zwahr C, Günther D, Brinkmann T, Gulow N, Oswald S, Grosse Holthaus M, Lasagni AF (2017) *Adv Healthc Mater* 6(3):27930868
12. Křenek T, Pola J, Docheva D, Stich T, Fajgar R, Kovářík T, Pola M, Martan J, Moskal D, Jandová V, Kupčák J, Mikysek P (2021) *Surf Interfaces* 26:101304
13. Fadeeva E, Chichkov B (2018) *Appl Sci* 8:1424
14. Clainche TL, Linklater D, Wong S, Le P, Juodkakis S, Le Guével X et al (2020) *ACS Appl Mater Interfaces* 12:48272–48283
15. Veiko VP, Karlagina YY, Itina TE, Kuznetsova DS, Elagin VV, Zagaynova EV et al (2021) *Opt Laser Technol* 138:106871
16. Gittens RA, McLachlan T, Olivares-Navarrete R, Cai Y, Berner S, Tannenbaum R, Schwartz Z, Sandhage KH, Boyan BD (2011) *Biomaterials* 32(13):3395–3403
17. Anisimov SI (1968) *Sov Phys JETP* 27:14–15
18. *Appl MAA* (2004) *Physica A* 79:997–999
19. Siuzdak K, Haryński L, Wawrzyniak J, Grochowska K (2021) *Prog Solid State Chem* 62:100297
20. Fathi-Hafshejani P, Johnson H, Ahmadi Z, Roach M, Shamsaei N, Mahjouri-Samani M (2020) *ACS Omega* 5(27):16744–16751
21. Burakov VS, Tarasenko NV, Savastenko NA (2001) *Spectrochim Acta B* 56(6):961–971
22. Parigger C, Woods A, Surmick D, Gautam G, Witte M (2015) *Hornkohl J Spectrochim Acta B* 107:132–138
23. Woods AC, Parigger CG, Hornkohl JO (2012) *J Opt Lett* 37:5139–5141
24. Itina TE, Hermann J, Delaporte P, Sentis M (2002) *Phys Rev E* 66:166406
25. Casavola AR, Colonna G, Cristofolini A, Borghi CA, Capitelli M (2008) *J Thermophys Heat Trans* 22:407–413
26. Yan Z, Mei X, Wang W, Pan A, Lin Q, Huang C (2019) *Opt Commun* 453:124384
27. Morozov AA, Geretovszky Z, Szörényi T (2008) *J Phys D* 41:015303
28. Tsalikis DG, Baig C, Mavrantzas VG, Amanatides E, Mataras D (2013) *J Chem Phys* 139:204706
29. <http://crystdb.nims.go.jp>. Accessed 4 2022
30. Xu Y, Yamazaki M, Villars P (2011) *Jpn J Appl Phys* 50:11RH02
31. Shabanov SV, Gornushkin IB (2014) *Spectrochim Acta B* 100:147–172
32. Shabanov SV, Gornushkin IB (2016) *Appl Phys A* 122:676
33. Gordon S, McBride BJ (1996) Computer program for calculation of complex chemical equilibrium compositions and applications: I. Analysis, II. User's Manual and Program Description, NASA Reference Publication 1311
34. Smith WR, Missen RW (1982) *Chemical reaction equilibrium analysis: theory and experiment*. Wiley, New York
35. Drawin HW (1976) *Pure Appl Chem* 48:133–153
36. Gornushkin IB, Veiko VP, Karlagina YY, Samokhvalov AA, Polyakov DS (2022) *Spectrochim Acta B*, in press
37. Parigger C, Woods A (2012) *AIP Conf Proc* 1464:628
38. De Giacomo A, Gaudiuso R, Dell'Aglio M, Santagata A (2010) *Spectrochim Acta B* 65:385–394
39. Lochte-Holtgreven W (1968) *Plasma diagnostics*. Wiley, New York
40. <https://www.nist.gov/pml/atomic-spectra-database>. Accessed 4 2022
41. Florian C, Wonneberger R, Undisz A, Kirner SV, Wasmuth K, Spaltmann D, Krüger J, Bonse J (2020) *Appl Phys A* 126:266
42. Syrtanov M, Garanin G, Kashkarov E, Pushilina N, Kudiyarov V, Murashkina T (2020) *Metals* 10:447–462
43. Han M-K, Im J-B, Hwang M-J, Kim B-J, Kim H-Y, Park Y-J (2015) *Metals* 5:850–862
44. Yan HH, Huang XC, Xi SX (2014) *Combust Explos Shock Waves* 50:192–195
45. Zhidkov MV, Golosov EV, Vershinina TN, Kudryashov SI, Kolobov YR, Ligachev AE (2018) *J Phys Conf Series* 1115:042066
46. Landis EC, Phillips KC, Mazur E, Friend CM (2012) *J Appl Phys* 112:063108
47. Michlíček M, Blahová L, Dvořáková E, Nečas D, Zajíčková L (2021) *Appl Surf Sci* 540:147979